Supplementary information

1

Evolution of the particle size distribution of tricalcium silicate during hydration by synchrotron X-ray nano-tomography

J. Neubauer [a*], T. Sowoidnich [b], L. Valentini [c], C. Schulbert [d], C. Naber [a], C. Rößler [b], J. Da Silva [e], F. Bellmann [b]

[a] Friedrich-Alexander Universitaet Erlangen-Nuernberg, GeoZentrum, Mineralogy, Schlossgarten 5a, 91054 Erlangen, Germany

[b] Bauhaus-Universitaet Weimar, Finger-Institute for Building Materials, Coudraystr. 11A, 99423 Weimar, Germany

[c] Università degli Studi di Padova, Department of Geosciences, 6 Via G. Gradenigo, 35131 Padua, Italy

[d] GeoZentrum Nordbayern, Section Palaeontology, Friedrich-Alexander Universitaet (FAU) Erlangen-Nuernberg, Loewenichstraße 28, 91054 Erlangen, Germany

[e] European Synchrotron Radiation Facility, 71 avenue des Martyrs, CS 40220, 38043 Grenoble Cedex 9, France

* corresponding author: juergen.neubauer@fau.de

Supplementary information

Table of contents:

Supplementary information

1. Supplementary information for the particle size distribution measured by laser diffraction and determined C_3S content measured by TA, ^{29}Si NMR and QXRD

The laser diffraction (measured by LS 230, Coulter with Polarization Intensity Differential Scattering (PIDS)) applied to the starting C_3S material reveals the following particle size distribution (Figure S1).
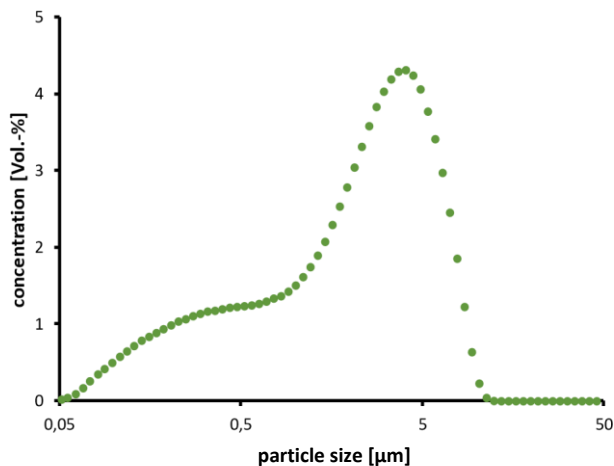

Figure S1: Particle size distribution of tricalcium silicate analyzed by laser diffraction.

By means of laser diffraction, it is revealed that the material is a relatively fine powder with 99.7 Vol.-% of particles having a diameter smaller than 10 µm and 85 Vol.-% of the particles having a diameter lower than 8 µm (Figure S1).

Table S1 reports the C_3S content in dependence of the hydration time determined by thermal analysis, ^{29}Si NMR, and QXRD.

Time	Thermal Analysis	^{29}Si NMR	QXRD	Mean value	Standard deviation
[h]	[wt.-%]	[wt.-%]	[wt.-%]	[wt.-%]	[wt.-%]
0	95.7	97.2	99.0	97.3	1.6
4	93.1	95.9	99.3	96.1	3.1
8	85.7	87.1	95.2	89.4	5.1
12	56.4	64.3	64.5	61.7	4.6
16	29.0	36.2	28.6	31.3	4.3
20	21.3	24.6	22.6	22.9	1.7
24	15.8	22.7	18.7	19.1	3.4

Table S1: C_3S-content in dependence of hydration time determined by different methods.

2. Supplementary information for synchrotron X-ray nano-tomography

2.1 Sample preparation and investigations

Supplementary information

A schematic illustration on the sample preparation steps and the nano-tomography as well as a simulation is shown in Figure S2
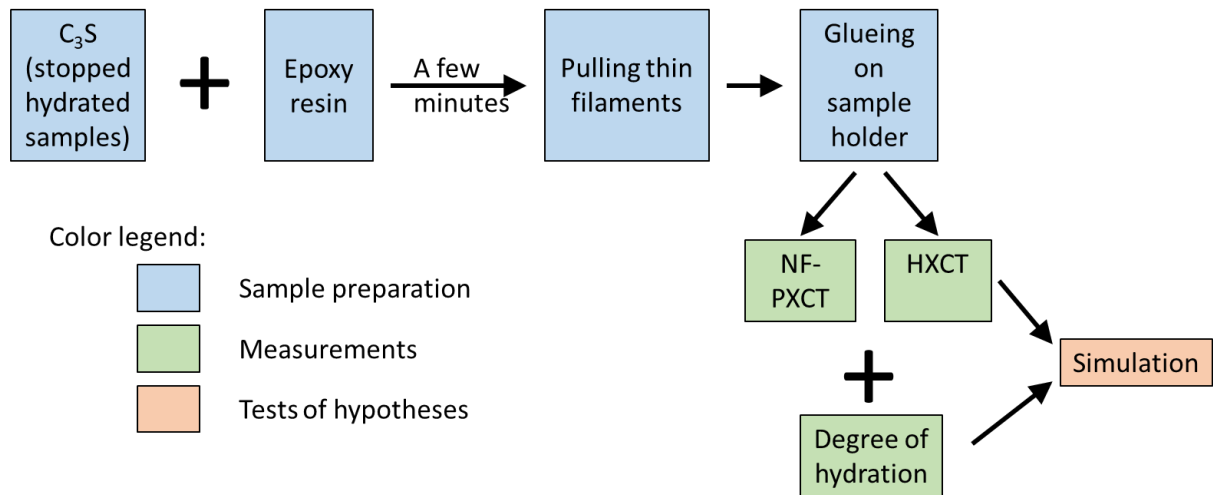

Figure S2: Sketch on the sample preparation and investigations regarding nano-tomography and simulation. NFPXCT: near-field ptychographic tomography, HXCT: holographic tomography.

2.2 Near-field ptychographic and holographic tomography experiments

The experiments were carried out at the ID16A nano-imaging beamline of the European Synchrotron Radiation Facility (ESRF) [1].

A FReLoN indirect detector system [2] with 4096 x 4096 pixels and a GGG: Eu scintillator was used. The physical pixel size of the CCD of 15 microns was magnified by 10x using an optics between the scintillator and the CCD. To be able to process the data, binned images by a factor 2, which resulted in a pixel size of 30 microns and arrays of 2048 x 2048 were acquired. The detector was located at $z12 = z1 + z2 = 1.208$ m downstream the X-ray focus position, where $z1$ is the focus-to-sample distance and $z2$ is the sample-to-detector distance. The sample was placed at $z1 = 20.13$ mm downstream the focus position. The divergence of the beam was of 5.5 mrad. Such a configuration yields acquired images with an effective pixel size of 50 nm due to the magnification of $z12/z1 = 60x$ of the divergent beam. The X-ray energy was set to 17.05 keV with 1% bandwidth.

For the near-field ptychography, the structures of multi-layered coating of the KB optics were used to create a structured beam required for the technique [3]. The tomographic scan was performed over 180 degrees using a binary acquisition strategy described by Kaestner et al. [4] with 4 nests of projections. 600 projections were acquired with angular steps of 0.3 degrees. Each ptychographic scan consisted of 17 pseudo-randomly distributed points with a maximum shift of 350 pixels [3] and the acquisition time of each scan point was 0.5 seconds. At each scan, 5 images without beam were acquired to take into account the dark noise of the detector. The average image of such 5 dark images was subtracted from the corresponding scan images.

For the holographic tomography experiments, each sample was scanned at 4 different sampleto-detector distances $z2$ [5]. At each distance, the sample was moved downstream the X-ray focus position while keeping the focus-detector distance $z12$ fixed. The values of $z1$ (sample-

focus distance) were: 0.015 mm, 0.016 mm, 0.020 mm, and 0.027 mm. These distances were chosen to achieve an effective pixel size of 50 nm. 800 projections were acquired over 180 degrees for each distance with an angular step of 0.225 degrees. A total of 3200 projections were therefore acquired with exposure time of 0.5 s which took about 3 h to complete. At each distance, 20 images without beam (dark images) and 21 images with beam but without sample (empty beam images) were also acquired. To prevent ring artefacts in the tomographic reconstructions, images using the random displacement method were acquired, which was based on displacing randomly the sample orthogonal to the incoming beam by 25 pixels between the successive tomographic projections [6].

2.3 Data processing

Near-field ptychographic tomography

The reconstruction of the 3D volume of each sample consisted of three steps: i) phase retrieval of each ptychographic scan; ii) pre-processing of each tomographic projection including registration of the misplacement of the sample at each angle; 3) tomographic reconstruction.

The phase retrieval was performed using the Python package Ptypy [7]. Due to the big size of the images, the data was firstly binned twice. 10,000 iterations of the difference map algorithm were used [8] to retrieve the phases. It was observed that some projections still displayed nonphysical phase vortices, indicating that the final convergence of the algorithm was not achieved yet. To deal with this problem, the non-physical vortices were removed as follows: i) the vortex positions and their corresponding topological charges were identified in each projection using the procedure described in previous works [9]; ii) the vortices were removed by multiplying them by a phase vortex of opposite topological charge at the same positions; iii) the resulting images were then casted into 2000 further iterations of the difference map algorithm until the proper convergence was reached. Since the vortices were not physical, they did not re-appear. Such a procedure has already been applied in previous works with cement [10].

Afterwards, the resulting images were interpolated back to the initial image size and used as initial guess to the difference map algorithm for 2,000 additional iterations without binning. This was followed by 300 iterations of the maximum likelihood refinement [11]. The resulting projections with a pixel size of 50 nm were processed and aligned for the tomographic reconstruction according to the methods previously described [12]. The tomographic reconstruction was performed on the phase projections using a modified filtered backprojection algorithm (FBP) using a Hilbert filter to circumvent phase unwrapping [12]. The final size of the reconstructed volumes was 2328 x 2357 x 2357 voxels, which corresponds to a volume of 116.4 x 117.85 x 117.85 μm$_3$.

Holographic tomography

The reconstruction of the 3D volume consisted of four steps: i) preparation of the image before the phase retrieval; ii) phase retrieval of each holographic scan consisting of image at 4 different sample-to-detector distances; iii) registration of the misplacement of the sample at each angle; iv) tomographic reconstruction.

Supplementary information

Before the phase retrieval, the average of the 20 dark images was subtracted from the corresponding scan images and empty beam images to take into account the dark noise of the detector. Afterwards, the scan images were divided by the average of the 21 empty beam images to remove the inhomogeneities of the incoming beam. The resulting projections were re-aligned with respect to the known random displacements that were applied during data acquisition. Subsequently, the projections at the four distances were interpolated to reach the pixel size of the images in the first distance.

The phase retrieval of the resulting projections with a pixel size of 50 nm was performed using the Contrast Transfer Function (CTF) approach [5] implemented in-house routing written in the GNU Octave programming environment and the public domain image analysis software ImageJ [13]. The final phase contrast projections were then aligned for the tomographic reconstruction. The tomographic reconstruction was carried out using the filtered back projection (FBP) algorithm [14] implemented in the ESRF software PyHST [15]. The final size of the reconstructed volumes was 2048 x 2048 x 2048 voxels, which corresponds to a volume of $(102.4)_3$ μm_3.

2.4 Data analysis

Near-field ptychographic tomography

For the inclusion/grain analysis, the ptychography data-sets were examined on a Windows 10 x64 workstation. The VGDefX-Algorithm from the Porosity/Inclusion Analysis Module of the software package VGSTUDIO MAX, version 3.1.0. was used. Volumes were imported in 16 bits, resulting in 65,536 different grey levels, where the lower grey levels represent less dense parts and the higher grey levels represent denser parts of the volume. Because of different 16-bit normalization value during the image processing, the grey levels of C_3S were defined to be in the range of 42,800 to 65,535 (0 h and 20 h) respectively from 49,500 to 65,535 (12 h and 16 h).

The resulting sub-volumes were then further analysed by the inclusion detection algorithm "VGDefX" with the analysis mode set to "inclusion", auto threshold mode "deviation", and a deviation factor of - 1.00. The analysis area from all of the original volumes was restricted because of a lower signal to noise ratio at the top of the scans. The algorithm produced distinct 3D shapes of C_3S, which were further used for the grain size distribution based on the diameter of the grain defined by the diameter of the virtual sphere around the grain. Lower grain size limit was fixed at a minimum volume of 8 voxels.

Holographic tomography

Image stacks reconstructed from the holo-tomographic scans relative to the reference sample and hydrated samples were processed using the freely available software ImageJ [13] with the aim of extrapolating the particle size distributions of C_3S. Conversion from grayscale to binary images was achieved using an adaptive local thresholding method [16] followed by noise removal using a selective median filtering.

3.   Supplementary information for ^{29}Si NMR spectroscopy

Supplementary information

The parameters used for the single-pulse ^{29}Si NMR experiments are reported in the main document. Figure S3 shows the ^{29}Si MAS NMR single-pulse spectra recorded for C_3S at various hydration times. Triclinic C_3S contains 9 different crystallographic silicon sites that can be resolved by NMR indicating chemical shifts between -68 and -75 ppm. The resonances of C-SH are much broader with Q_1 at approximately -79 ppm and Q_2 at approximately -85 ppm. It can be seen that the intensity of the C_3S resonances decreases with hydration time, whereas the C-S-H intensity increases.
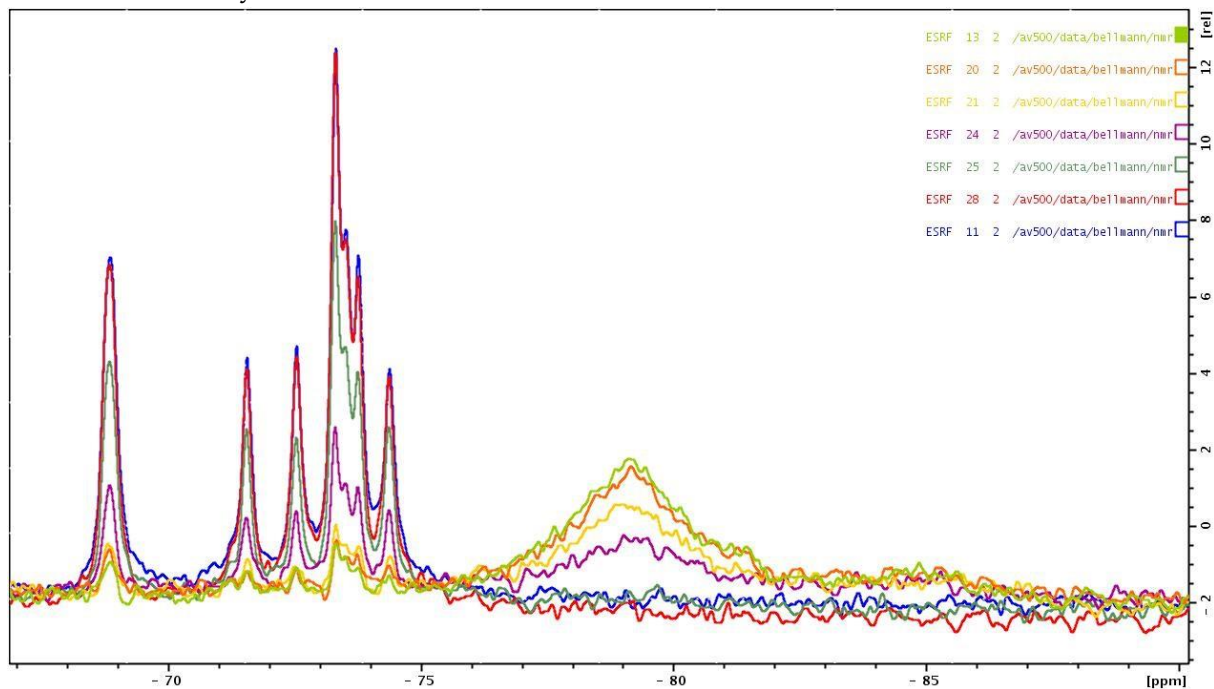

Figure S3: ^{29}Si single pulse NMR spectra of C_3S after 0 h, (blue), 4 h (red), 8 h (green), 12 h (pink), 16 h (yellow), 20 h (orange) and 24 h (olive) of hydration.

Besides the single-pulse, also cross-polarization (CP) experiments were conducted for selective observation of silicon in the near vicinity of hydrogen. The parameters used for the ^{29}Si{^{1}H} CP experiments are reported in the main document.

The concentration of hydrated material with Q_0-sites has been quantified in previous studies from CP data assuming that Q_0 corresponds to a metastable C-S-H phase containing isolated silicon tetrahedra. For quantification of the amount of metastable C-S-H the Q_0 intensities were extracted and implemented in calculations using the molar weight of metastable C-S-H (169 g/mol). The latter is based on the formula $1.3\,CaO \cdot SiO_2 \cdot 2H_2O$ with the Ca/Si-ratio estimated elsewhere [17] .

The deconvolution of the ^{29}Si{^{1}H} CP-NMR spectra provides the intensities of the hydrated material. However, this relies on the assignment of chemical shifts for the individual silicon sites and such data can be extracted from a fit of the CP spectra (Figure S4) and is provided in Table S2 for Q_0, Q_1 and Q_2 sites.
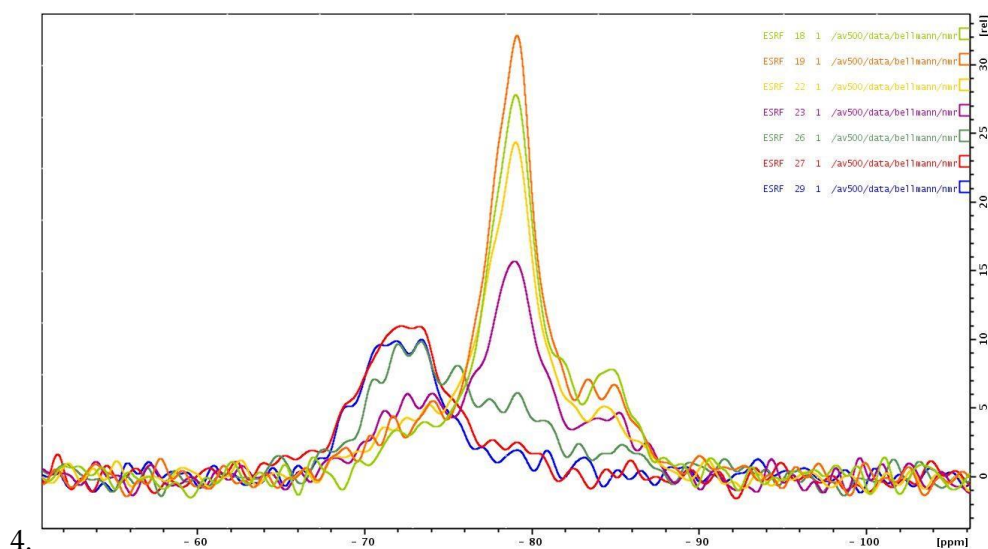
4.

Figure S4: ^{29}Si{^{1}H} CP spectra of anhydrous C_3S (blue), 4 h hydrated (red), 8 h hydrated (green), 12 h hydrated (pink), 16 h hydrated (yellow), 20 h hydrated (orange) and 24 h hydrated (olive). The relative amplitude depends also on the amount of material in the rotor and the concentration of the individual phases is extracted from the deconvolution.

It can be seen from Table S2 that two distinct resonances were observed for Q_0, Q_1, and Q_2 sites, which have a fairly constant chemical shift when considering that the FWHM of theses resonances is 100 to 300 Hz.

	Chemical shift for Q_0-sites [ppm]	Chemical shift for Q_1-sites [ppm]	Chemical shift for Q_2-sites [ppm]
Starting material	-71.0, -73.5	-75.6, -79.1	
4 h hydrated	-71.0, -73.4	-75.6, -79.2	
8 h hydrated	-71.0, -73.4	-75.6, -79.2	-81.0, -85.3
12 h hydrated	-71.2, -74.0	-76.5, -79.0	-81.3, -84.5
16 h hydrated	-71.3, -73.8	-77.5, -79.1	-81.8, -84.5
20 h hydrated	-71.7, -74.0	-77.5, -79.1	-81.8, -83.4, -85.0
24 h hydrated	-71.8, -73.6	-77.4, -79.1	-81.9, -84.7

Table S2: Chemical shift data extracted from the CP experiments for Q_0, Q_1 and Q_2 resonances in the hydrated samples

Hydrated Q_0 sites were detected even before the hydration experiment was started, indicating that grinding and air classification have resulted in the absorption of water from the atmosphere. Such resonances of Q_0-sites in close vicinity to hydrogen have been observed in a number of previous NMR investigations [18-21]. It has been discussed in those studies that such resonances can be associated to a superficially hydroxylated surface of C_3S or the presence of a metastable C-S-H. The clear identification of these resonances in the CP spectra and the very small FWHM (mean value 21 Hz) of the resonances of C_3S, which overlap with the hydrated material, allowed the quantification of the concentration of the metastable C-SH in these samples from the single-pulse spectra for these samples. The results indicate that

the concentration of metastable C-S-H is between 0.9 and 1.1 wt.-% in the first 8 hours. A higher value is observed after 12 hours (1.5 wt.-%) but the concentration falls during the deceleration period (0.7 wt.-% after 16 hours and 0.3 wt.-% after 20 and 24 hours).

Additionally, two resonances were extracted for Q_1 and Q_2-sites, which are clearly associated to stable C-S-H. The first observation of Q_1 is after 4 h hydration, whereas Q_2-sites are detected after 8 h and later. Therefore, the single pulse ^{29}Si MAS NMR spectra allowed for the first time a direct quantification of the concentration of the metastable hydrate phase containing silicon tetrahedra in Q_0 coordination, which has been based on cross polarization techniques in previous studies [18, 20, 21].

4. Supplementary information for the aqueous phase composition

A possible explanation for the measured ion concentrations in the aqueous phase during hydration can be obtained by the plot of silicon against calcium, see Figure S5.
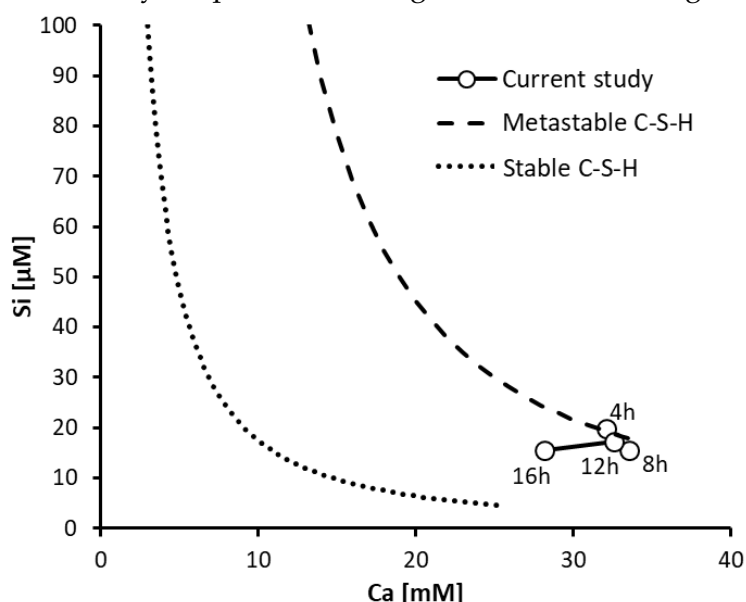

Figure S5: Aqueous phase composition during hydration of C_3S (points) with the solubility curves of stable (dotted line) [22] and metastable C-S-H (dashed line) [17].

In Figure S5, the solubility curves of metastable [17] and stable C-S-H [22] are additionally provided. It can be seen that up to 12 h hydration the aqueous phase composition lie relatively close to the solubility curve of the metastable C-S-H. However, it departs from this line at later hydration times and the solution lies significantly below the metastable solubility curve after 16 hours.

5. Supplementary references

1. Cesar da Silva, J., et al., *Efficient concentration of high-energy x-rays for diffraction-limited imaging resolution.* Optica, 2017. **4**(5): p. 492-495.
2. Labiche, J.-C., et al., *Invited article: The fast readout low noise camera as a versatile x-ray detector for time resolved dispersive extended x-ray absorption fine structure and diffraction studies of dynamic problems in materials science, chemistry, and catalysis.* Review of Scientific Instruments, 2007. **78**(9): p. 091301.

Supplementary information

3.   Stockmar, M., et al., *Near-field ptychography: phase retrieval for inline holography using a structured illumination.* Scientific Reports, 2013. **3**: p. 1927.

4.   Kaestner, A.P., B. Munch, and P. Trtik, *Spatiotemporal computed tomography of dynamic processes*. Vol. 50. 2011: SPIE. 10.

5.   Mokso, R., et al., *Nanoscale zoom tomography with hard x rays using Kirkpatrick-Baez optics.* Applied Physics Letters, 2007. **90**(14): p. 144104.

6.   Hubert, M., et al., *Efficient correction of wavefront inhomogeneities in X-ray holographic nanotomography by random sample displacement.* Applied Physics Letters, 2018. **112**(20): p. 203704.

7.   Enders, B. and P. Thibault, *A computational framework for ptychographic reconstructions.* Proceedings of the Royal Society A: Mathematical, Physical and Engineering Sciences, 2016. **472**(2196): p. 20160640.

8.   Thibault, P., et al., *Probe retrieval in ptychographic coherent diffractive imaging.* Ultramicroscopy, 2009. **109**(4): p. 338-343.

9.   Goldstein, R.M., H.A. Zebker, and C.L. Werner, *Satellite radar interferometry: Twodimensional phase unwrapping.* Radio Science, 1988. **23**(4): p. 713-720.

10.   Cuesta, A., et al., *Chemistry and Mass Density of Aluminum Hydroxide Gel in Eco-Cements by Ptychographic X-ray Computed Tomography.* The Journal of Physical Chemistry C, 2017. **121**(5): p. 3044-3054.

11.   Thibault, P. and M. Guizar-Sicairos, *Maximum-likelihood refinement for coherent diffractive imaging.* New Journal of Physics, 2012. **14 063004**.

12.   Guizar-Sicairos, M., et al., *Phase tomography from x-ray coherent diffractive imaging projections.* Optics Express, 2011. **19**(22): p. 21345-21357.

13.   Schneider, C.A., W.S. Rasband, and K.W. Eliceiri, *NIH Image to ImageJ: 25 years of image analysis.* Nature Methods, 2012. **9**: p. 671.

14.   Bracewell, R.N. and A.C. Riddle, *Inversion of Fan-Beam Scans in Radio Astronomy.* Astrophysical Journal, 1967. **150**: p. 427.

15.   Mirone, A., et al., *The PyHST2 hybrid distributed code for high speed tomographic reconstruction with iterative reconstruction and a priori knowledge capabilities.* Nuclear Instruments and Methods in Physics Research Section B: Beam Interactions with Materials and Atoms, 2014. **324**: p. 41-48.

16.   Neerad, P., et al. *Adaptive local thresholding for detection of nuclei in diversity stained cytology images*. in *2011 International Conference on Communications and Signal Processing*. 2011.

17.   Sowoidnich, T., et al., *New insights into tricalcium silicate hydration in paste.* Journal of the American Ceramic Society, 2019. **102**(5): p. 2965-2976.

18.   Rodger, S.A., et al., *Hydration of Tricalcium Silicate Followed by 29Si NMR with CrossPolarization.* Journal of the American Ceramic Society, 1988. **71**(2): p. 91-96.

19.   Damidot, D. and A. Nonat, *C3S hydration in diluted and stirred suspensions: (II) properties of C-S-H precipitated during the two kinetic steps.* Advances in Cement Research, 1994. **6**(22): p. 83-91.

20.   Bellmann, F., et al., *Improved evidence for the existence of an intermediate phase during hydration of tricalcium silicate.* Cement and Concrete Research, 2010. **40**(6): p. 875-884.

21.   Pustovgar, E., et al., *Understanding silicate hydration from quantitative analyses of hydrating tricalcium silicates.* Nat Commun, 2016. **7**: p. 10952.

22.   Haas, J. and A. Nonat, *From C–S–H to C–A–S–H: Experimental study and thermodynamic modelling.* Cement and Concrete Research, 2015. **68**(0): p. 124-138.